

Revealing Nanoscale Chemical Heterogeneities in Polycrystalline Mo-BiVO₄ Thin Films

Johanna Eichhorn, Sebastian E. Reyes-Lillo, Subhayan Roychoudhury, Shawn Sallis, Johannes Weis, David M. Larson, Jason K. Cooper, Ian D. Sharp, David Prendergast, and Francesca M. Toma*

The activity of polycrystalline thin film photoelectrodes is impacted by local variations of the material properties due to the exposure of different crystal facets and the presence of grain/domain boundaries. Here a multi-modal approach is applied to correlate nanoscale heterogeneities in chemical composition and electronic structure with nanoscale morphology in polycrystalline Mo-BiVO₄. By using scanning transmission X-ray microscopy, the characteristic structure of polycrystalline film is used to disentangle the different X-ray absorption spectra corresponding to grain centers and grain boundaries. Comparing both spectra reveals phase segregation of V₂O₅ at grain boundaries of Mo-BiVO₄ thin films, which is further supported by X-ray photoelectron spectroscopy and many-body density functional theory calculations. Theoretical calculations also enable to predict the X-ray absorption spectral fingerprint of polarons in Mo-BiVO₄. After photo-electrochemical operation, the degraded Mo-BiVO₄ films show similar grain center and grain boundary spectra indicating V₂O₅ dissolution in the course of the reaction. Overall, these findings provide valuable insights into the degradation mechanism and the impact of material heterogeneities on the material performance and stability of polycrystalline photoelectrodes.

In this context, photo-electrochemical (PEC) water splitting is a promising approach to convert sunlight directly into storable, energy-dense fuels, and has the potential to provide a large fraction of current and future energy demands. For this application, a highly investigated photo-electrode material is bismuth vanadate (BiVO₄), which is characterized by a theoretical photocurrent density of 7.5 mA cm⁻² that corresponds to a solar-to-hydrogen conversion efficiency of up to 9.2%.^[2] However, the performance of BiVO₄ photoanodes commonly falls significantly below this theoretical efficiency limit due to low electronic mobility, recombination, and trapping of photogenerated charges.^[3] Additionally, parallel (photo)corrosion processes in this material affect sustained performance, thus limiting long term durability.^[4]

In polycrystalline systems, variations of the material properties across the photo-electrode can impact PEC activity and stability due, for example, to the presence of


different exposed crystal facets or of structural imperfections, such as domain and grain boundaries.^[5] Whereas previous studies have elucidated the correlation between charge transport characteristics and morphological changes at the nanoscale,^[3a,4a] the impact of spatially heterogeneous chemical composition and electronic structure on the material stability is still largely

1. Introduction

Addressing the consequences of climate change caused by the increasing consumption of fossil fuels is one of the pressing global challenges. To overcome the current reliance on fossil fuels, a transition to a carbon neutral society will be crucial.^[1]

Dr. J. Eichhorn, J. Weis, D. M. Larson, Dr. J. K. Cooper, Prof. I. D. Sharp, Dr. F. M. Toma
Chemical Sciences Division and Joint Center for Artificial Photosynthesis
Lawrence Berkeley National Laboratory
1 Cyclotron Road, Berkeley, CA 94720, USA
E-mail: fmtoma@lbl.gov

Dr. J. Eichhorn, Prof. I. D. Sharp
Walter Schottky Institut und Physik Department
Technische Universität München
Am Coulombwall 4, Garching 85748, Germany

 The ORCID identification number(s) for the author(s) of this article can be found under <https://doi.org/10.1002/smll.202001600>.

© 2020 The Authors. Published by Wiley-VCH GmbH. This is an open access article under the terms of the Creative Commons Attribution License, which permits use, distribution and reproduction in any medium, provided the original work is properly cited.

Prof. S. E. Reyes-Lillo
Departamento de Ciencias Físicas
Universidad Andres Bello
Santiago 837-0136, Chile

Dr. S. Roychoudhury, Dr. S. Sallis
Advanced Light Source
Lawrence Berkeley National Laboratory
Berkeley, CA 94720, USA

Dr. S. Roychoudhury, Dr. D. Prendergast
The Molecular Foundry
Lawrence Berkeley National Laboratory
Berkeley, CA 94720, USA

DOI: 10.1002/smll.202001600

unknown. Elucidating such local composition-reactivity relationships is essential for addressing fundamental degradation mechanisms and provides a route to improving device stability and efficiency at the macroscale.

In this context, scanning transmission X-ray microscopy (STXM) is a powerful technique to locally resolve variations in the electronic and chemical structure of materials with a lateral resolution of ≈ 10 nm.^[6] STXM has previously been applied in battery research to study the insertion and extraction of lithium ions from nanostructured electrodes,^[7] as well as in the context of fuel cell research to characterize the local chemical environment of catalyst nanoparticles.^[8]

Here, we apply a general multimodal approach that combines the unique features of STXM with atomic force microscopy (AFM) to determine relationships between local chemical composition, electronic structure, and nanoscale morphology of advanced photoelectrodes, using sputtered Mo-BiVO₄ thin films as a model system. Specifically, we combine spatially resolved X-ray absorption spectra obtained by STXM to provide information about changes in the chemical composition and electronic structure, with the corresponding Mo-BiVO₄ film morphology obtained by atomic force microscopy. Using the power of STXM as a spectromicroscopic technique, we disentangle the different X-ray absorption spectra corresponding to grain centers and grain boundaries compositions of the Mo-BiVO₄ film. We find that the absorption spectrum at grain centers corresponds to Mo-BiVO₄, whereas the spectrum at grain boundaries indicates the presence of V₂O₅. These results are also supported by X-ray photoelectron spectroscopy (XPS). Many-body density functional theory (DFT) calculations of the O K-edge absorption spectra for Mo-BiVO₄ and V₂O₅ provide further understanding of the chemical composition in heterogeneous regions within the thin film probed by experimental measurements. As polarons are known to affect metal oxide properties such as efficiency,^[2a] in this study DFT calculations are also used to predict the spectral fingerprint of polarons in the X-ray absorption spectrum. This multimodal approach enables the precise assignment of structural features to its absorption properties. Additionally, STXM analysis of ex situ degraded Mo-BiVO₄ films after PEC operation were investigated to provide insight into the degradation mechanism and to reveal the impact of material heterogeneities on the material stability. After degradation, the X-ray absorption spectra of the grain center and the grain boundaries are similar, indicating that V₂O₅ is dissolved in the course of the photo-electrochemical reaction. Overall, elucidation of local variation in the chemical composition and electronic structure of polycrystalline photoelectrodes provides valuable insights for understanding the dominating process limiting the material stability and performance, which in turn can support the rational design of photoelectrodes with controlled composition, defects, and disorder.

2. Results and Discussion

2.1. Evaluation of Mo-BiVO₄ on ITO-Substrate and SiN_x-Window

We have chosen Mo-BiVO₄ thin films as a model system to understand the correlation between chemical composition, electronic structure, and nanoscale morphology. Doping with

high valent transition-metal cations, such as W or Mo, has been shown to enhance the PEC performance of BiVO₄ by increasing its conductivity.^[9] Nevertheless, both doped and undoped photoelectrodes suffer from significant photo-electrochemical instability under operational conditions.^[4a,10] Here, STXM is used to elucidate the chemical composition and the electronic structure of polycrystalline Mo-BiVO₄ thin films via collection of elemental maps and local X-ray absorption spectra with 10 nm lateral resolution. For PEC characterization, Mo-BiVO₄ is typically deposited on transparent conductive oxides (TCO). In order to prevent spectral overlap of the O K-edge of the TCO and of the Mo-BiVO₄ during STXM measurements, we deposited Mo-BiVO₄ thin films directly on SiN_x windows by reactive magnetron cosputtering. In parallel, Mo-BiVO₄ thin films were deposited on indium tin oxide (ITO) using an identical protocol in order to characterize photo-electrochemical properties of the material. After deposition, the thin films deposited on both substrates were annealed in H₂ atmosphere at ≈ 260 °C for 15 min.^[11]

The overall composition of the Mo-BiVO₄ thin films was analyzed by inductively coupled plasma mass spectrometry (ICP-MS), revealing Mo-doping concentrations of about 4%. The corresponding X-ray diffraction (XRD) patterns of Mo-BiVO₄ films on ITO and Mo-BiVO₄ films on SiN_x exhibit the characteristic peak structures of monoclinic scheelite phase of BiVO₄ (Figure S1, Supporting Information). On both substrates, scanning electron microscopy (SEM) indicates a dense polycrystalline structure with grain sizes between 50 and 200 nm (Figure S2, Supporting Information). Subsequently, the photo-electrochemical performance of as-grown Mo-BiVO₄/ITO photoelectrodes was verified by cyclic voltammetry (CV) in 1 M potassium phosphate (KPi) buffer at pH 6.8 in the presence of 0.1 M sodium sulfite as hole scavenger in dark and under illumination (AM 1.5, 100 mW cm⁻², Figure S3a, Supporting Information). We also evaluated the stability of the Mo-BiVO₄ photoanodes by chronoamperometry (Figure S3b, Supporting Information). Compared to as-grown Mo-BiVO₄, the degraded thin films exhibit lower photocurrents and anodic shifts in the photocurrent onset potentials. Additionally, SEM images following degradation show the formation of voids between single grains, indicating the dissolution of the Mo-BiVO₄ film (Figure S2c, Supporting Information). Dissolution of Mo-BiVO₄ is also supported by the loss of Bi and V, as evidenced by analysis of the elemental surface composition obtained with XPS (Table S1, Supporting Information). Overall, the observed decrease in PEC performance and associated morphological changes are in good agreement with our previous study on photocorrosion of undoped BiVO₄ thin films in near-neutral environments.^[4a]

Analogue degradation experiments were conducted on Mo-BiVO₄ on SiN_x windows, which were specially prepared for STXM measurements. While a bias can be applied to Mo-BiVO₄/ITO substrates to drive the photo-electrochemical reaction, the absence of an underlying TCO film does not provide this possibility for the case of Mo-BiVO₄/SiN_x. However, we have previously reported that pristine BiVO₄ degrades under illumination at E_{oc} , thus without applying a bias. Degradation of pristine BiVO₄ under illumination yields to a reduced corrosion rate relative to degradation under anodically biased electrodes, thus longer times are needed in order to achieve a similar degree of degradation.^[4a] Therefore, the Mo-BiVO₄ films on

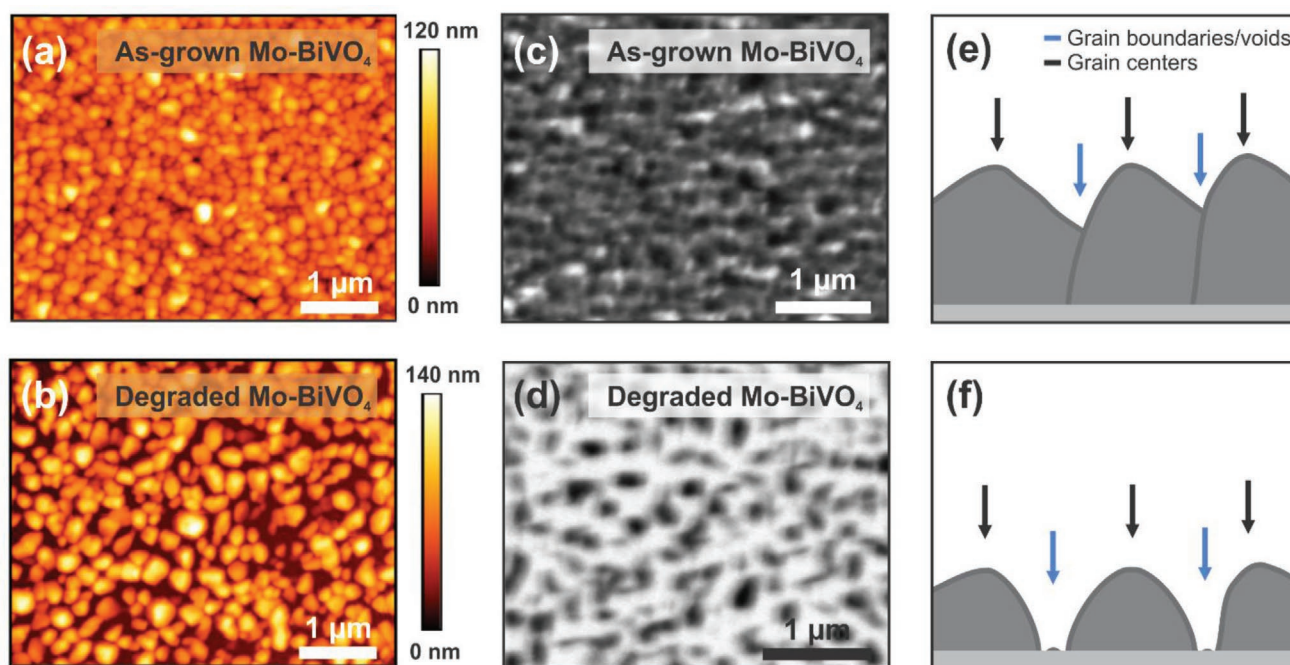


Figure 1. Nanoscale morphology and chemical heterogeneity of Mo-BiVO₄ thin films. AFM images of a) as-grown and b) degraded Mo-BiVO₄ thin films on SiN_x windows. After degradation, the grains become disconnected from each other due to material dissolution at grain boundaries. X-ray absorption maps at the V L₃-edge (519 eV) of c) the as-grown and d) the degraded Mo-BiVO₄ thin films on SiN_x windows. The dark areas correspond to strong absorption, whereas the bright areas indicate high transmission. Schematic of the grain structure within the e) as-grown and f) degraded Mo-BiVO₄ thin film highlighting grain centers and grain boundaries.

SiN_x windows were illuminated in 1 M KPi at pH 6.8 without an applied bias for ≈12 h to achieve a degree of decomposition similar to that one obtained by photo-electrochemical degradation of Mo-BiVO₄/ITO photoelectrodes. Representative AFM images of the as-grown and the degraded Mo-BiVO₄ film on SiN_x windows are shown in **Figure 1a,b**. Similar to the experiments using Mo-BiVO₄ films on ITO (Figure S2, Supporting Information), voids are formed within the films after degradation (Figure 1b), whereas the as-prepared samples are characterized by a dense film structure (Figure 1a). Small features with a height below 3 nm are observed between voids in the degraded sample. These features can be assigned to partially dissolved grains.

2.2. Correlation between Nanoscale Morphology and Chemical Heterogeneity in Mo-BiVO₄ Thin Films

To elucidate local changes within as-grown as well as degraded Mo-BiVO₄ films (90 nm thickness), we recorded laterally resolved STXM maps at different photon energies, hereafter referred to as energy stacks. The energy stacks span the V L- and O K-edges corresponding to photon energies of 515–528 eV and 529–550 eV, respectively. For both samples, representative X-ray absorption maps at 519 eV (V L₃-edge) are shown in Figure 1c,d and reveal heterogeneities within the thin films. In both maps, dark areas indicate high X-ray absorption and thus low X-ray transmission, whereas bright areas correspond to low X-ray absorption and thus high X-ray transmission. Generally, the polycrystalline structure of Mo-BiVO₄ films comprise grains and grain boundaries between neighboring grains as

highlighted in the schematic shown in Figure 1e,f for as-grown and degraded Mo-BiVO₄ thin films, respectively. For both films, we can correlate the film morphology and the contrast within the X-ray transmission maps (Figure 1a,b vs Figure 1c,d) to assign dark areas to grain centers and bright areas to grain boundaries (and to voids for degraded samples), as highlighted by black and blue arrows in Figure 1e,f, respectively.

The recorded X-ray absorption spectra of Mo-BiVO₄ in **Figure 2** are characterized by the vanadium L-edge and the oxygen K-edge. We provide the analysis and comparison of these spectra with existing literature on un-doped and doped Mo-BiVO₄, as well as V₂O₅.^[2b,12] While in V₂O₅ the coordination geometry of the oxygen ligands is octahedral, in Mo-BiVO₄ is tetrahedral. In detail, the V spectrum comprises the L₃- (515–520 eV) and L₂-edge (521–528 eV), which are separated by ≈6.8 eV due to the spin-orbit coupling of the 2p core hole.^[2b,12] The L₃-edge arises from dipole-allowed transition from V 2p_{3/2} core levels to the unoccupied V 3d states of the conduction band (CB). Within the V L₃-region, three main peaks are discernable at 516.3 eV (t₂, Peak 2), 517.3 eV (Peak 3), and 518.5 eV (e, Peak 4) originating from the ligand field splitting of V 3d states.^[2b,12] Specifically, the peak at 516.3 eV (Peak 2) is composed of V 3d_{z²} and 3d_{x²-y²} states, and the peak at 518.5 eV (Peak 4) of V 3d_{xy}, 3d_{yz}, and 3d_{zx} states.^[13] A small shoulder is observed at a photon energy of ≈515.3 eV (Peak 1), which can be attributed to core hole exciton or to excitation of an electron into a small polaronic state at V⁴⁺ sites generated by Mo-doping.^[12,14] An additional feature at 519.7 eV (Peak 5) is a consequence of mixing of anisotropic Bi 6p states with O 2p states.^[12] The V L₂-region corresponds to excitation from

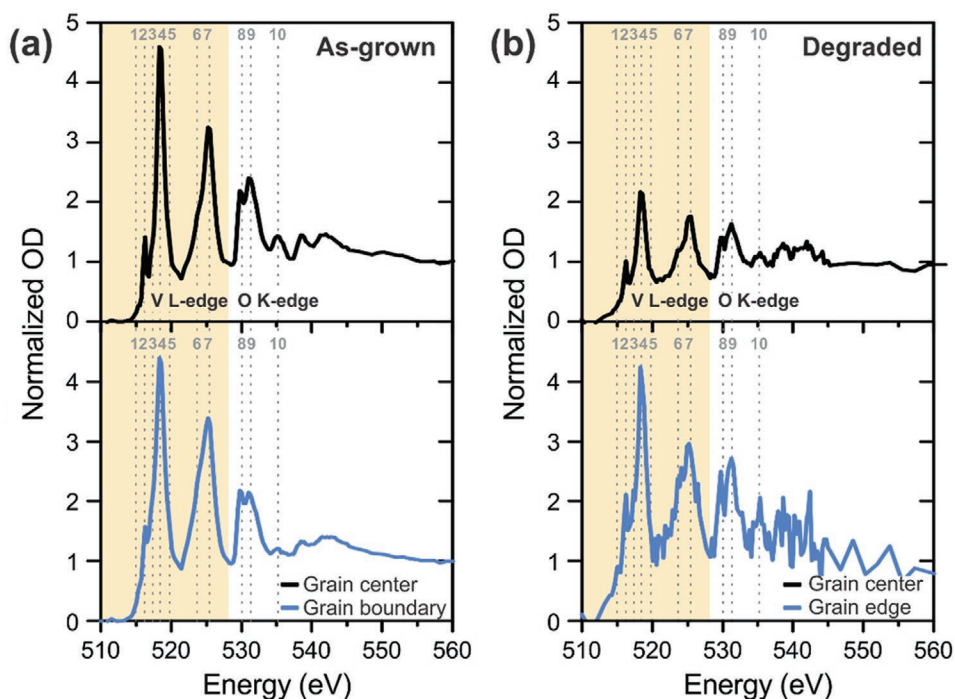


Figure 2. Analysis of nanoscale chemical heterogeneity in Mo-BiVO₄ grains. X-ray absorption spectra of a) as-grown and b) degraded Mo-BiVO₄ thin films extracted from the energy stack by masking areas with lower and higher absorption. Considering the film morphology, the spectra are considered to be representative for the spectrum at the grain center (black) and at the grain boundaries (blue) of the polycrystalline films, respectively. In the extracted absorption spectra, pre-edge background subtraction and post-edge step normalization were carried out.

2p_{1/2} core levels to unoccupied CB V 3d states, which is further split into two peaks at 523.5 eV (Peak 6) and 525.3 eV (Peak 7) corresponding to t₂ and e states, respectively. A Coster–Kronig Auger decay process from a 2p_{1/2} into a 2p_{3/2} hole renders the V L₂ feature less informative due to the associated increase in spectral broadening.^[7a,12] The O K-edge is adjacent to the V L_{2/3}-edge. The O K-edge involves transitions from occupied O 1s core levels to empty O 2p states, thus providing an insight into unoccupied metal states due to hybridization with oxygen valence states.^[12,14] The spectrum can be deconvoluted into three components at 530.9 eV (Peak 8), 532.1 eV (Peak 9), and 535.1 eV (Peak 10). Characteristic peaks at 530.9 eV (Peak 8) and 532.1 eV (Peak 9) are associated with hybridization of O 2p states with vanadium t₂ and e states.^[2b] The spectral components at 535.1 eV (Peak 10) is related to hybridized O 2p and Bi 6p states.^[2b,12] Beyond 538 eV a broad extended band indicates mixing of metal 4 sp and O 2p electrons.

Further, analysis of the energy stacks (laterally resolved STXM maps for different photon energies) highlights the presence of regions of the samples with different chemical composition. In order to provide an accurate analysis, we first carried out image post-processing of the energy stacks and identified areas with low and high X-ray absorption intensity. The extracted spectra shows differences between grain boundaries (low absorption) and central regions of the grains

(high absorption). Representative spectra for the as-grown and degraded Mo-BiVO₄ are shown in Figure 2a,b and Table 1.

To independently infer the main spectral components that could be extracted by analysis of the images, we also carried out principle component analysis (PCA) on the energy stack of the as-grown and degraded sample. In this way, it is possible to accurately deconvolve the relevant spectral components, and to exactly assign spectral changes to specific variation in the chemical composition across the sample. The dataset of the as-grown and degraded Mo-BiVO₄ samples reveals four components, where only two regions shows a significant spectral signature (Figure 3a,b and Figure S4, Supporting Information). To assign the morphological character to the two main spectral components, we plotted the fractional contribution of each component to the overall spectrum at each pixel (Figure 3c,d, and Figures S5–S7, Supporting Information). For degraded Mo-BiVO₄ (Figure 3c,d), the distribution of component 1 (Figure 3a) shows bright round spots indicating the high contribution at the center of the grain. In contrast, the distribution of component 2 (Figure 3b) is mainly characterized by bright circles reflecting the high contribution of the grain boundaries. Notably, there is excellent agreement between the distinct regions identified by PCA and those ones identified by the energy stack post-processing approach, thus confirming that we can discern between grain centers and grain boundaries.

Table 1. Summary of XAS peaks in the V L- and O K-regions.

	Peak 1	Peak 2	Peak 3	Peak 4	Peak 5	Peak 6	Peak 7	Peak 8	Peak 9	Peak 10
Energy (eV)	515.3	516.3	517.3	518.5	519.7	523.5	525.3	530.9	532.1	535.1

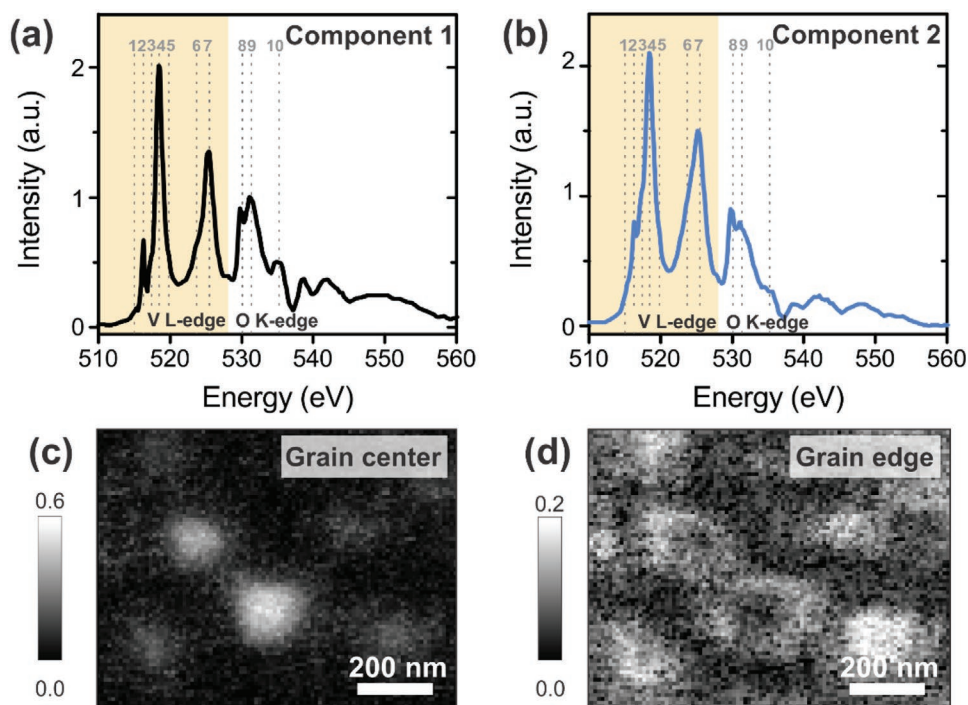


Figure 3. Principle component analysis of Mo-BiVO₄ energy stacks. a) Component 1 and b) component 2 of the absorption spectra for degraded Mo-BiVO₄ obtained from PCA. Spatial distribution of the fractional contribution of component 1 and 2 to the overall spectrum. Component 1 corresponds to the grain center, whereas component 2 represents the grain edges.

The comparison of grain centers and grain boundaries X-ray absorption spectra of as-grown Mo-BiVO₄ thin films (Figure 2a) highlights changes in both the V L- and in the O K-edge. With respect to the spectrum at the grain center, the spectrum at the grain boundaries shows increased peak intensities in the V L-regions between 515 eV (Peak 1) and 518 eV (Peak 4) as well as 523 eV (Peak 6) and 525 eV (Peak 7). These changes are accompanied by a decrease in peak intensity at 535.1 eV (Peak 10) in the O K-edge. The peak at 535.1 eV (Peak 10) arises from O 2p-Bi 6p states and its disappearance indicates that these states are more pronounced in the center spectrum compared to the grain boundaries. In the O K-edge, the intensity ratio of the two peaks at 530.9 eV (Peak 8) and 532.1 eV (Peak 9) is reversed. In contrast, the spectrum at the grain boundaries reveals similar intensities for both peaks.

X-ray absorption spectra for degraded Mo-BiVO₄ were also extracted from energy stacks (Figure 2b). Generally, the thickness of the thin film is clearly reduced after degradation, which leads to a lower signal to noise ratio. In contrast to as-grown Mo-BiVO₄, no significant spectral changes are observed between the grain center and the grain boundaries of degraded Mo-BiVO₄. In particular, in both spectra the peak at 532.1 eV (Peak 9) is more intense compared to the peak at 530.9 eV (Peak 8), indicating the presence of BiVO₄ at the grain center and at the grain boundaries. A recent study showed that the L₃/L₂ peak ratio increases for decreasing oxidation states of the vanadium.^[15] Comparing the peak ratios for center (1.2) and boundary (1.4) of degraded Mo-BiVO₄ suggest a decrease in the oxidation state of vanadium at the grain boundaries, which

could arise from the reaction with the electrolyte or the creation of additional defect.

X-ray photoelectron spectroscopy can provide further information on the surface composition of as-grown and degraded Mo-doped BiVO₄ films (Figure 4 and Table S1, Supporting Information). For as-grown Mo-BiVO₄, the binding energy (BE) of Bi 4f_{7/2} is ≈159.1 eV and can be assigned to the presence of Bi³⁺ ions, which is in agreement with previous reports on stoichiometric BiVO₄ films and single crystals.^[4a,12,16] In the corresponding V 2p_{3/2} spectrum, three different spectral components can be identified at binding energies of 515.7, 516.8, and 517.7 eV. In agreement with literature,^[4a,12,16] the peak at 516.8 eV can be assigned to V⁵⁺ states in BiVO₄. Furthermore, the peak at 517.7 eV can be attributed to the presence of V⁵⁺ ions in V₂O₅. This observation is in agreement with previous reports on sputtered vanadium-rich Mo-BiVO₄, which revealed phase segregation of V₂O₅ within the BiVO₄ layer.^[16] Lastly, the V 2p_{3/2} spectrum also reveals a small shoulder at 515.7 eV corresponding to the presences of V⁴⁺ states in BiVO₄. Such V⁴⁺ is commonly observed on BiVO₄ surface and is typically assigned to the presence of defects, e.g., oxygen vacancies.^[15,17] For Mo-BiVO₄, the formation of V⁴⁺ states can also arise from Mo-doping,^[12,18] when an electron is donated from Mo⁶⁺ dopants to V⁵⁺ lattice sites. In the Mo 3d spectrum (Figure S8, Supporting Information), the Mo 3d_{5/2} peak was centered at about 232.4 eV, which is consistent with the Mo-dopant being in the +6 oxidation state in the BiVO₄ lattice.^[9b,12]

While the as-grown BiVO₄ spectrum shows only one doublet in the Bi 4f spectrum, the Bi 4f spectrum of degraded Mo-BiVO₄ is composed of two doublets (Figure 4c). In the V 2p spectrum, we

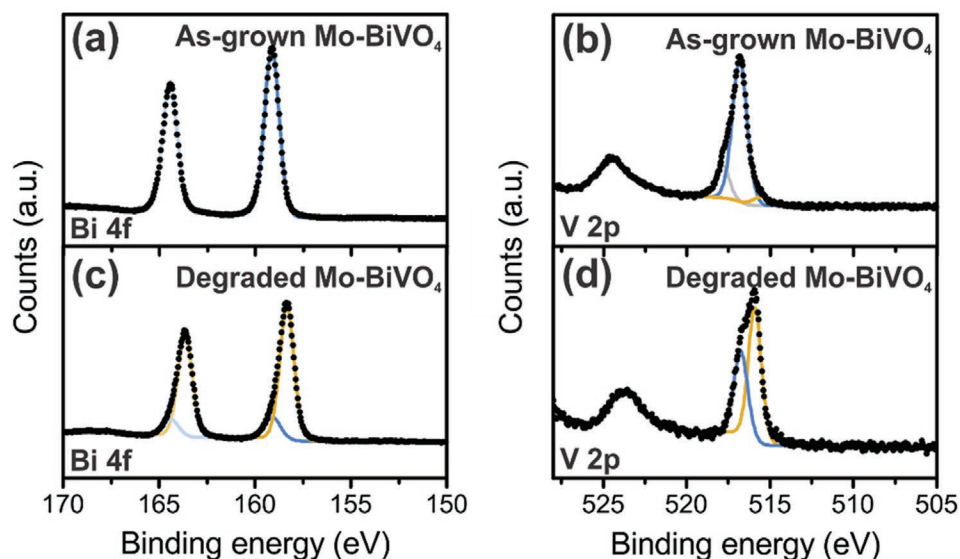


Figure 4. Surface composition of Mo-BiVO₄ thin films. a,c) Bi 4f and b,d) V 2p core level X-ray photoelectron spectra of pristine and degraded Mo-BiVO₄ on ITO-coated glass substrate.

also observe the formation of a second species after degradation. The emergence of these components indicate chemical changes to the surface after PEC operation. Similar shifts toward lower binding energies were also reported for dark and photocharged BiVO₄ tested in electrolyte solution,^[15] as well as for the deposition of different metal oxide layers on BiVO₄.^[19] In addition, it is important to note that the peak at 517.7 eV in the V 2p spectrum is absent after PEC degradation, confirming the removal of V₂O₅ from the surface during photo-electrochemical operation.

According to our XPS results, one reason for the change of the XAS intensity ratio of the two peaks at 530.9 and 532.1 eV for the center and boundary component could be the presence of V₂O₅ at the grain boundaries of as-grown Mo-BiVO₄ thin films. In V₂O₅, the coordination geometry of the oxygen ligands is octahedral, whereas it is tetrahedral in Mo-BiVO₄. The change from tetrahedral to octahedral can lead to different shapes of the V L-edge due to the inversion of the d orbital splitting.^[12] Compared to BiVO₄, the XAS spectrum of V₂O₅^[12] exhibits increased peak intensities at the low photon energy side of the V L₃- and L₂-edge as well as higher intensities of the peak at 530.9 eV (Peak 8) relative to the peak at 532.1 eV (Peak 9) in the O K-region. The characteristic spectrum of V₂O₅ is in agreement with the spectrum of component 2 determined by PCA (Figure S4, Supporting Information).

2.3. Origin of Chemical Heterogeneity in Mo-BiVO₄ Thin Films

In order to test the hypothesis that the presence of V₂O₅ lead to the observed spectral changes within the thin film in the X-ray absorption spectra, we simulated the O K-edge XAS spectra of Mo-doped BiVO₄ and V₂O₅ using the many-body Δ SCF determinant formalism and crystalline atomic structure configurations without thermal effects (see details in the Experimental Section). These spectra are aligned to the same energy reference.^[20] The many-body XAS (MBXAS) determinant

formalism provides considerable insight into the origins of O K-edge spectral features in terms of chemical and orbital contributions due to hybridization between oxygen and transition metal valence states. The computed MBXAS spectrum of Mo-BiVO₄ reproduces the prominent near-edge peaks at 529.6, 530.6, and 533.2 eV (Figure 5 and Figures S9 and S10,

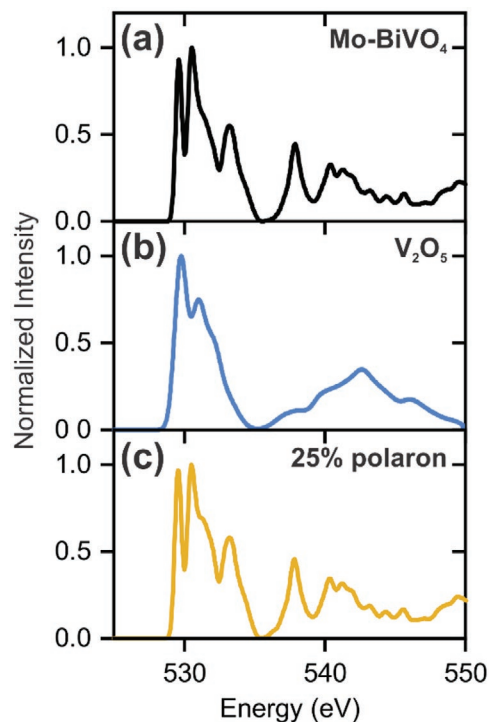


Figure 5. MBXAS simulations. a) Simulated O K-edge XAS spectrum for Mo-BiVO₄ and b) V₂O₅. The spectra are properly aligned with respect to the same reference. The first peak is seen to coincide for the two structures. c) Effect of 25% polaron and Mo-doping on the MBXAS spectra of Mo-BiVO₄.

Supporting Information), in excellent agreement with the O K-edge of the experimental spectrum of the grain centers at 530.9 eV (Peak 8), 532.1 eV (Peak 9), and 535.1 eV (Peak 10, Figure 2). Additionally, the computed MBXAS spectrum of Mo-BiVO₄ reproduces the relative peak intensity between the first two near-edge peaks, thus providing insight into the local electronic and chemical structure. The experimentally derived intensity ratio of 1.091 is in good agreement with the theoretically calculated value of 1.084. The origin of the underestimation can be traced back to localization effects of the Hubbard U correction and a simultaneous underestimation of the monoclinic distortion ($\gamma = 90.03$) compared to experiments ($\gamma = 90.38$).^[21]

The calculated O K-edge XAS spectrum of V₂O₅ is in good agreement with experimental results (Figure 5 and Figure S11, Supporting Information).^[7a,12] By comparing the spectrum of V₂O₅ to experiments, we find that the MBXAS spectrum of V₂O₅ reproduces the main peak at 529.8 eV as well as the relative intensity between the first peak at 529.8 eV and the second peak at 531.0 eV. Notably, the high-intensity first peak of V₂O₅ coincides with the first peak of Mo-BiVO₄, and in contrast to the case of Mo-BiVO₄, the second peak displays a considerably smaller intensity than the first peak. Furthermore, the V₂O₅ spectrum has a sharp decrease in intensity above the second peak shoulder around 532.0 eV. Hence, the simultaneous presence of Mo-BiVO₄ and V₂O₅ may lead to an overall increase of intensity across the spectrum, with a higher intensity increase around the first peak of Mo-BiVO₄ and a relatively smaller intensity increase around and above the second peak of Mo-BiVO₄. This prediction is in good agreement with the behavior observed for the experimental O K-edge spectrum at the grain boundaries of Mo-BiVO₄. The experimental spectrum at the grain boundaries of as-grown Mo-BiVO₄ can be explained by assuming a convolution of the V₂O₅ and Mo-BiVO₄ spectra, supported by an increased relative peak intensity at 530.9 eV (Peak 8) and at 532.1 eV (Peak 9), respectively (Figure 2a and Table S2, Supporting Information). Accordingly, the higher-intensity first-peak in the O K-region for the spectrum at the grain boundaries compared to the spectrum at the grain center is a direct result of contributions from V₂O₅. Overall, our study reveals the presence of a mixed V₂O₅ and Mo-BiVO₄ composition at the grain boundaries, whereas the grain center is composed of Mo-BiVO₄. These results complement our previous findings on the chemical transformation of BiVO₄.^[4a] We hypothesize that the presence of V₂O₅ at the grain boundaries in BiVO₄ might facilitate the dissolution during photo-electrochemical degradation. Specifically, when V₂O₅ is located at grain boundaries and subsequently chemically etched due to its instability, the apparent surface area per geometric area of the sample is increased. This increase of the BiVO₄/electrolyte contact area, especially at previously unexposed grain edges, it is expected to lead to more rapid dissolution than would be expected for otherwise densely packed films. This finding is in agreement with our previous study, which indicates that the dissolution of the BiVO₄ thin film initiates at solid/liquid interfaces and is accelerated in the presence of voids.^[4a]

After providing an interpretation of the observed X-ray absorption spectral changes, we have applied MBXAS to

predict the spectral feature of the polaron character in the X-ray absorption experimental spectrum of Mo-BiVO₄ (Figure 5). Electron small polarons, which are strongly localized charges at individual sites that cause lattice distortions, have been often correlated with materials limitations in metal oxides.^[22] Specifically, after doping, the photo-electrochemical performance of undoped BiVO₄ is typically improved.^[16,23] This improvement is commonly assigned to increased charge carrier concentration rather than to increased mobility. While both charge carrier concentration and mobility would lead to higher conductivity, the latter is rather related to electron small polarons.^[9] Capturing formation of polarons experimentally is challenging^[12] and requires minimum concentration of dopants, here we propose first principles DFT simulations to predict the experimental X-ray absorption spectral feature as a function of both polaron and/or dopant concentration, and calculate the formation and hopping energies of polarons in Mo-doped BiVO₄ (see Figure 5 and Figures S12 and S13, Supporting Information). We find that upon replacement of a V atom with a Mo impurity in the supercell, the additional electron provided by Mo⁵⁺ is localized as a polaron in a V-site. Interestingly, we notice that the polaron becomes less stable with decreasing distance from the Mo atom (Table S3, Supporting Information). This finding supports that increasing Mo-doping concentration induces polaron delocalization in the ground state structure, thus suggesting an increase in electron mobility in BiVO₄ with increasing Mo-doping concentration. In addition, the predicted peak intensity ratio provides insight into the local electronic and chemical structure of the VO₄ tetrahedron, which is affected by the concentration of polarons and Mo-impurities introduced in the lattice (Figure 5). A large concentration of polarons and/or Mo impurities can be artificially simulated as a weighted average between the MBXAS spectrum of Mo-BiVO₄ and that obtained upon excitation of an oxygen atom either next to the polaron and/or the Mo impurity. If the polaron concentration is artificially increased, by linearly increasing the MBXAS contribution from the excited oxygen near the polaron, we find that the intensity of the first near-edge peak decreases (see Figure S12, Supporting Information). In contrast, the same computational experiment for an excited oxygen near the Mo impurity leads to a slight increase of the first peak and a sizeable transfer of spectral weight from the second peak toward its shoulder, considerably reducing the size of the second peak and developing a new third peak in the position of the original second's peak shoulder (see Figure S13, Supporting Information). Our results suggest that the latter effect dominates over the former (see Figure S14, Supporting Information), and that the concentration of Mo-impurities would need to go as high as 10% to induce a visible change in the STXM measurements of Mo-BiVO₄. While this concentration is higher compared to our results ($\approx 4\%$ by ICP-MS), these findings shows the predicted polaron spectral feature in the X-ray absorption spectrum of Mo-BiVO₄ and confirm that high doping level can increase electron mobility by destabilization of electron small polarons.^[2a] These predictions indicate that it is possible to identify polaronic features in the X-ray absorption spectrum of Mo-BiVO₄, whereas the high concentration of Mo which is required may at the same time exacerbate the phase segregation of V₂O₅.

3. Conclusion

In summary, we used STXM to locally resolve variations in chemical composition and electronic structure within sputtered Mo-doped BiVO₄ photoelectrodes. We utilized the correlation between the morphology of polycrystalline thin films and the contrast within the X-ray transmission maps to extract the X-ray absorption spectra at the grain center and at the grain boundaries from the measured STXM energy stacks. Comparison of spectra obtained from grain centers with those ones obtained at grain boundaries revealed phase segregation of V₂O₅ in the Mo-BiVO₄ film, which was further supported by XPS and MBXAS calculations. Additionally, STXM was conducted on ex situ degraded Mo-BiVO₄ to gain insights into the degradation process. The degraded Mo-BiVO₄ films showed similar X-ray absorption spectra at the grain center and at the grain boundary indicating the dissolution of the segregated V₂O₅ phase. MBXAS also allows to predict the X-ray absorption spectral feature of polarons in the O K-edge as a function of Mo-doping in the material. This work motivates further STXM measurements under in situ and operando conditions to monitor the local chemical variations under PEC operation. These operando measurements will enable the detection of metastable chemical species which would only form in the photo-electrochemical environment. Improved understanding of the degradation pathway will aid the development and design of passivation and protection layers to realize efficient and stable photoelectrodes.

4. Experimental Section

Sample Preparation: Polycrystalline Mo-BiVO₄ thin films were deposited on indium tin oxide (ITO)-coated glass substrates (Delta Technologies, LTD, CB-40IN) for PEC measurements and on SiN_x windows (Norcada NX5100C) for STXM measurements. For the synthesis, the previously reported procedure for reactive co-sputtering of Mo-BiVO₄ thin films was adapted to the experimental setup.^[23] The thin films were synthesized in LAB Line sputtering system (Kurt J. Lesker) using a chamber pressure of 10 mTorr with 7% oxygen and 93% argon. For this work, a co-sputtering approach was applied using three separate targets for Bi₂O₃ (99.9%), V (99.99%), and Mo (99.99%). Furthermore, the sputtering rates were controlled independently with three different target power supplies for Bi, V, and Mo. Similar to previous reports,^[16,23] a high-power direct current (DC) power supply was used for the V target and a radio frequency (RF) power supply for the Bi₂O₃ and Mo targets to achieve good compositional control. Specifically, 280 W was used for the V DC power supply, 13 W for the Bi₂O₃, and 5 W for the Mo RF power supply. During deposition, the substrate was heated to 450 °C. The film thicknesses on ITO-coated glass substrates and on the SiN_x windows were ≈60 and ≈90 nm, respectively. Following deposition, all samples were annealed in a quartz glass tube furnace equipped with a vacuum pump and mass flow controllers for flowing N₂ and H₂ gases. The Mo-BiVO₄ films were annealed in 1 atm of H₂ with a flow rate of 150 sccm at 263 °C for 15 min. After annealing, the furnace was opened to cool the samples to room temperature.

Material Characterization: The bulk compositions of the prepared Mo-BiVO₄ thin films were quantified by inductively coupled plasma mass spectroscopy (7900 ICP-MS, Agilent) following digestion of films with concentrated HNO₃. In the following, the Mo-doping concentration is defined as the ratio of Mo/(Mo+V) to account for the atomic substitution ratio of vanadium V⁵⁺ with molybdenum Mo⁶⁺ in the BiVO₄ bulk lattice. The ICP-MS results reveal a Mo-doping concentration of ≈4% and a V/(V+Bi+Mo) ratio of 0.51.

The crystalline phase and phase purity were analyzed by grazing incident and Bragg-Brentano X-ray diffraction using a Rigaku SmartLab X-ray diffractometer with Cu K_α radiation. The morphologies of the as-grown and degraded Mo-BiVO₄ thin films were evaluated by means of scanning electron microscopy (SEM, FEI Quanta 250 FEG) and atomic force microscopy (AFM, Bruker Dimension Icon) before and after stability testing. All AFM measurements were performed with silicon probes with a nominal spring constant of 0.4 N m⁻¹ (scansyst-air). The topographic images were recorded at the center of the SiN_x window.

Photo-Electrochemical Characterization and Degradation: All photo-electrochemical measurements were performed in a three-electrode cell using a Ag/AgCl reference electrode (3 M NaCl), the Mo-BiVO₄ thin film photoanode as working electrode and a Pt-wire as counter electrode. Cyclic voltammetry was conducted in 1 M KPi buffer at pH 6.8 with 0.1 M sodium sulfite as sacrificial reagent. For stability tests and material degradation, chronoamperometry was performed at pH 6.8 in the absence of sodium sulfite. The degradation of Mo-BiVO₄ thin films on ITO was conducted with an applied bias of 1.23 V versus reversible hydrogen electrode (RHE), whereas the degradation of Mo-BiVO₄ thin films on SiN_x windows was performed at E_{oc}. The performance of Mo-BiVO₄ thin films on ITO was evaluated before and after 1 h stability testing. All measurements were performed under illumination using simulated AM 1.5 light adjusted to 100 mW cm⁻².

Scanning Transmission X-Ray Microscopy: For STXM measurements, Mo-BiVO₄ thin films were directly sputtered on SiN_x windows. STXM was conducted at the undulator beamline 11.0.2 of the Advanced Light Source (ALS, Lawrence Berkeley National Laboratory, USA) using 90% circularly polarized light. Monochromatic X-rays from the beamline illuminate a zone plate lens with an outer zone diameter of 25 nm to focus the beam. Details of the STXM instrumentation, operating procedures, and analysis methodology are reported in detail in ref. [24]. All STXM measurements were performed in helium atmosphere after an initial pump down to ≈10⁻² mTorr. The samples were scanned with a focused X-ray beam with photon energies of 510 to 575 eV and the transmitted X-rays were detected to generate image sequences, referred to as energy stacks. The energy step size was varied across the energy stack, whereby ≈0.8 eV is used from 510 to 514 eV (pre-edge), 0.25 eV from 514 to 545 eV (main peaks) and 1.75 eV from 545 to 575 eV (post-edge). For Mo-BiVO₄, image stacks across the vanadium L-edge and oxygen K-edge were acquired on different samples and at different regions within each sample. STXM was conducted on as-grown as well as ex situ degraded Mo-BiVO₄ films. Prior to STXM measurements, the degraded samples on SiN_x were carefully rinsed with deionized water and dried in ambient air to ensure the integrity of the SiN_x window.

Since the thin film covered the whole SiN_x-window, it was necessary to measure the reference spectrum of a plain SiN_x-window separately on a different sample. Therefore, a plain SiN_x-window was mounted alongside the Mo-BiVO₄ samples on the same sample holder. All samples were introduced in the STXM chamber at the same time to ensure identical measurement conditions. All STXM data were analyzed and processed using aXis2000 software (<http://unicorn.mcmaster.ca/aXis2000.html>). The recorded images within a stack were aligned using the cross-correlation algorithm implemented in aXis2000 and the transmitted signal was converted to optical density. Absorption spectra at grain boundaries and grain center were extracted from the energy stack by masking regions with lower and higher absorption, respectively. Subsequently, these masks were applied to extract the average spectra for these regions. Standard pre-edge background subtraction and post-edge step normalization procedures are applied to the extracted absorption spectra. To determine the absorption peak positions, the extracted absorption spectra were fitted with Gaussian peaks.

Principal Component Analysis: The STXM image stacks were arranged into a matrix such that each pixel of the image was assigned to a single column and the spectra constructed by the image stack at that pixel was placed into the corresponding row. Principle component analysis was used to determine the number of latent sources via inspection of the eigenvalues, the imbedded error (IE) function. The sources

themselves were estimated using a Bayesian nonnegative matrix factorization (NNMF) algorithm which constrains the latent sources and the fractional abundances to be positive while also constraining the sum of the fractional abundances to be one as required by the physics of transmission spectroscopy. The algorithm uses a Gibbs sampler to simulate posterior distributions for the latent sources and the fractional abundances. The constraints imply that the latent sources form a simplex around the data in an $N-1$ dimensional space where N is the number of latent sources as determined via PCA. Additional constraints are added to the latent source prior in order to minimize the volume of the simplex and to prevent the estimated sources from straying too far from the available data. The Bayesian NNMF algorithm was used to estimate four latent sources two of which are associated with the background. The final estimate of the latent sources and fractional abundances was taken to be the mean of the posterior distributions generated via the Bayesian NNMF algorithm. Images representing a segmentation of the original STXM data were reconstructed using the estimated fractional abundances additionally the intensity of the background sources was used to estimate the relative heights.

X-Ray Photoelectron Spectroscopy: The near-surface composition was determined by X-ray photoelectron spectroscopy measurements using a monochromatized Al $K\alpha$ source ($h\nu = 1486.6$ eV) and pass energy of 20 eV on a Kratos Axis Ultra DLD system. Core level spectra for Bi 4f, V 2p, Mo 3d, O 1s, and C 1s was collected. Survey spectra collected on a typical sputtered Mo-BiVO₄ sample (data not shown) can show additional peaks from the substrate. Spectral positions were corrected using adventitious carbon by shifting the C 1s core level position to 284.8 eV. For calculating the surface atomic composition of as-grown Mo-BiVO₄, the peak area of V 2p_{3/2} and Bi 4f_{7/2} were used, weighted by the corresponding atomic sensitivity factors. Spectral fitting was conducted using Casa XPS analysis software. The XPS data indicate that as-grown BiVO₄ has a V/(V+Bi+Mo) ratio of ≈ 0.44 . The results are in agreement with previous studies reporting a Bi-rich surface for un-doped BiVO₄ thin films and single crystals.^[7,19,20] However, bulk-sensitive X-ray diffraction confirmed the formation of monoclinic scheelite phase. Additionally, the Mo-doping concentration (Mo)/(Mo+V) at the surface is calculated to be less than 0.1, which is at the detection limit of the instrument.

First Principles Calculations: The structure of Mo-doped BiVO₄ is simulated by replacing one V atom with one Mo atom in a large supercell of the BiVO₄ lattice. Ground state DFT calculations are performed with Quantum ESPRESSO.^[25] The generalized gradient approximation of Perdew, Burke, and Ernzerhof (PBE)^[26] plus the Hubbard U (PBE+U) method^[27] was used to properly describe the localized d orbitals of Mo-BiVO₄. The Hubbard U values for V and Mo, $U_V = 3$ eV and $U_{Mo} = 4$ eV respectively, are chosen according to the literature.^[28] The calculations use a kinetic energy cut off of 30 Ry, a charge-density cut off of 300 Ry, and ultrasoft pseudopotential with 15, 14, 13, and 6 explicit valence electrons for Bi ($5d^{10}6s^26p^3$), Mo ($4s^24p^64d^55s^1$), V ($3s^23p^63d^34s^2$), and O ($2s^22p^4$), respectively.^[29] Supercell structural relaxations are performed with $2 \times 2 \times 2$ k-point grids until forces are smaller than 2.5×10^{-3} eV Å⁻¹.

XAS spectra are simulated using the many-body Δ SCF determinant formalism (MBXAS).^[30] The calculations use a $1 \times 1 \times 1$ Γ -centered k-point grid for supercell electronic structure calculations and computed spectra are convoluted with a Gaussian broadening of 0.2 eV. The core-excited electronic structure and associated orbitals used in spectral line-shape calculations are computed from the full-core hole (FCH) approximation.^[31] The spectra for different materials and for different excited sites within the same material have been aligned with respect to the same many-body energy reference by calculating the absorption onset-energy within the excited-electron and core hole (XCH) approximation.^[32] The large supercell limit of the many-body XAS (MBXAS) spectra is computed by exciting the oxygen atom located at the farthest transition metal site from both the defect as well as from the polaron, if the latter is localized. The 1s core-excited O atom is simulated using a pseudo-potential with electronic configuration $1s^12s^22p^4$. Convergence studies performed for the X-ray absorption spectrum of BiVO₄ with respect to supercell size and k-point grid show that a supercell structure of 96 atoms is enough to converge the spectrum

and provide results in agreement with experiments. The supercell lattice parameters are sufficiently large to neglect effects from the core-hole impurity with neighboring periodic images.

Supporting Information

Supporting Information is available from the Wiley Online Library or from the author.

Acknowledgements

This study was supported by the Laboratory Directed Research and Development Program of Lawrence Berkeley National Laboratory under U.S. Department of Energy contract number DE-AC02-05CH11231. This research used resources of the Advanced Light Source, a U.S. DOE Office of Science User Facility under contract no. DE-AC02-05CH11231. Theory work at the Molecular Foundry was supported by the Office of Science, Office of Basic Energy Sciences, of the U.S. Department of Energy under Contract No. DE-AC02-05CH11231. The synthesis of bismuth vanadate was supported by the Joint Center for Artificial Photosynthesis, a DOE Energy Innovation Hub, supported through the Office of Science of the U.S. Department of Energy under Award Number DE-SC0004993. J.E. acknowledges funding by the Deutsche Forschungsgemeinschaft (DFG, German Research Foundation) - 428591260. S.E.R.-L. acknowledges support from DGI-UNAB Regular Grant No. DI-21-18/"REG" and FONDECYT Iniciación en Investigación Grant No. 11180590. I.D.S. acknowledges funding by the DFG under Germany's Excellence Strategy - EXC 2089/1 - 390776260. The authors acknowledge Dr. Mary K. Gilles for beamline support, help with STXM measurements, and useful discussions; Dr. David Vine and Dr. David Shapiro for beamline support; and Dr. Matthew L. Snedaker for preliminary experimental support. Prof. Will Chueh and Dr. Liming Zhang are greatly acknowledged for helpful discussions.

Conflict of Interest

The authors declare no conflict of interest.

Keywords

bismuth vanadate, chemical heterogeneity, first principles, scanning X-ray microscopy, water splitting

Received: March 10, 2020

Revised: June 4, 2020

Published online: August 5, 2020

- [1] S. Chu, Y. Cui, N. Liu, *Nat. Mater.* **2017**, *16*, 16.
- [2] a) I. D. Sharp, J. K. Cooper, F. M. Toma, R. Buonsanti, *ACS Energy Lett.* **2017**, *2*, 139; b) J. K. Cooper, S. Gul, F. M. Toma, L. Chen, P.-A. Glans, J. Guo, J. W. Ager, J. Yano, I. D. Sharp, *Chem. Mater.* **2014**, *26*, 5365.
- [3] a) J. Eichhorn, C. Kastl, J. K. Cooper, D. Ziegler, A. M. Schwartzberg, I. D. Sharp, F. M. Toma, *Nat. Commun.* **2018**, *9*, 2597; b) A. J. E. Rettie, W. D. Chemelewski, D. Emin, C. B. Mullins, *J. Phys. Chem. Lett.* **2016**, *7*, 471; c) J. Eichhorn, C. Kastl, A. M. Schwartzberg, I. D. Sharp, F. M. Toma, *ACS Appl. Mater. Interfaces* **2018**, *10*, 35129.
- [4] a) F. M. Toma, J. K. Cooper, V. Kunzelmann, M. T. McDowell, J. Yu, D. M. Larson, N. J. Borys, C. Abelyan, J. W. Beeman,

- K. M. Yu, J. Yang, L. Chen, M. R. Shaner, J. Spurgeon, F. A. Houle, K. A. Persson, I. D. Sharp, *Nat. Commun.* **2016**, *7*, 12012;
- b) J. Eichhorn, G. Liu, F. M. Toma, in *Integrated Solar Fuel Generators*, The Royal Society of Chemistry, London **2019**, p. 281.
- [5] P. Chakthranont, L. C. Seitz, T. F. Jaramillo, *J. Phys. Chem. Lett.* **2015**, *6*, 3702.
- [6] a) J. Stöhr, *NEXAFS Spectroscopy*, Springer-Verlag, Berlin Heidelberg **1992**; b) M. Abbate, H. Pen, M. T. Czyżyk, F. M. F. de Groot, J. C. Fuggle, Y. J. Ma, C. T. Chen, F. Sette, A. Fujimori, Y. Ueda, K. Kosuge, *J. Electron Spectrosc. Relat. Phenom.* **1993**, *62*, 185.
- [7] a) L. R. De Jesus, G. A. Horrocks, Y. Liang, A. Parija, C. Jaye, L. Wangoh, J. Wang, D. A. Fischer, L. F. J. Piper, D. Prendergast, S. Banerjee, *Nat. Commun.* **2016**, *7*, 12022; b) J. Lim, Y. Li, D. H. Alsem, H. So, S. C. Lee, P. Bai, D. A. Cogswell, X. Liu, N. Jin, Y.-s. Yu, N. J. Salmon, D. A. Shapiro, M. Z. Bazant, T. Tylliszczak, W. C. Chueh, *Science* **2016**, *353*, 566.
- [8] J. Wang, J. Zhou, Y. Hu, T. Regier, *Energy Environ. Sci.* **2013**, *6*, 926.
- [9] a) F. F. Abdi, S. P. Berglund, *J. Phys. D: Appl. Phys.* **2017**, *50*, 193002; b) K. P. S. Parmar, H. J. Kang, A. Bist, P. Dua, J. S. Jang, J. S. Lee, *ChemSusChem* **2012**, *5*, 1926.
- [10] X. Yao, X. Zhao, J. Hu, H. Xie, D. Wang, X. Cao, Z. Zhang, Y. Huang, Z. Chen, T. Sritharan, *iScience* **2019**, *19*, 976.
- [11] J. K. Cooper, S. B. Scott, Y. Ling, J. Yang, S. Hao, Y. Li, F. M. Toma, M. Stutzmann, K. V. Lakshmi, I. D. Sharp, *Chem. Mater.* **2016**, *28*, 5761.
- [12] M. Favaro, R. Uecker, S. Nappini, I. Piš, E. Magnano, H. Bluhm, R. van de Krol, D. E. Starr, *J. Phys. Chem. C* **2019**, *123*, 8347.
- [13] Z. Zhao, Z. Li, Z. Zou, *Phys. Chem. Chem. Phys.* **2011**, *13*, 4746.
- [14] L. F. J. Piper, A. DeMasi, S. W. Cho, A. R. H. Preston, J. Laverock, K. E. Smith, K. G. West, J. W. Lu, S. A. Wolf, *Phys. Rev. B* **2010**, *82*, 235103.
- [15] N. J. Firet, A. Venugopal, M. A. Blommaert, C. Cavallari, C. J. Sahle, A. Longo, W. A. Smith, *Chem. Mater.* **2019**, *31*, 7453.
- [16] L. Chen, E. Alarcón-Lladó, M. Hettick, I. D. Sharp, Y. Lin, A. Javey, J. W. Ager, *J. Phys. Chem. C* **2013**, *117*, 21635.
- [17] M. D. Rossell, P. Agrawal, A. Borgschulte, C. Hébert, D. Passerone, R. Erni, *Chem. Mater.* **2015**, *27*, 3593.
- [18] a) V. Jovic, J. Laverock, A. J. E. Rettie, J. S. Zhou, C. B. Mullins, V. R. Singh, B. Lamoureux, D. Wilson, T. Y. Su, B. Jovic, H. Bluhm, T. Söhnel, K. E. Smith, *J. Mater. Chem. A* **2015**, *3*, 23743; b) T. Liu, X. Zhou, M. Dupuis, C. Li, *Phys. Chem. Chem. Phys.* **2015**, *17*, 23503.
- [19] Y. Hermans, S. Murcia-López, A. Klein, R. van de Krol, T. Andreu, J. R. Morante, T. Toupance, W. Jaegermann, *Phys. Chem. Chem. Phys.* **2019**, *21*, 5086.
- [20] a) A. H. England, A. M. Duffin, C. P. Schwartz, J. S. Uejio, D. Prendergast, R. J. Saykally, *Chem. Phys. Lett.* **2011**, *514*, 187; b) P. Jiang, D. Prendergast, F. Borondics, S. Porsgaard, L. Giovanetti, E. Pach, J. Newberg, H. Bluhm, F. Besenbacher, M. Salmeron, *J. Chem. Phys.* **2013**, *138*, 024704.
- [21] A. W. Sleight, H. y. Chen, A. Ferretti, D. E. Cox, *Mater. Res. Bull.* **1979**, *14*, 1571.
- [22] M. Reticcioli, U. Diebold, G. Kresse, C. Franchini, in *Handbook of Materials Modeling* (Ed: S. Y. W. Andreoni), Springer, Cham **2019**.
- [23] L. Chen, F. M. Toma, J. K. Cooper, A. Lyon, Y. Lin, I. D. Sharp, J. W. Ager, *ChemSusChem* **2015**, *8*, 1066.
- [24] a) A. P. Hitchcock, C. Morin, X. Zhang, T. Araki, J. Dynes, H. Stoeber, J. Brash, J. R. Lawrence, G. G. Leppard, *J. Electron Spectrosc. Relat. Phenom.* **2005**, *144*, 259; b) A. L. D. Kilcoyne, T. Tylliszczak, W. F. Steele, S. Fakra, P. Hitchcock, K. Franck, E. Anderson, B. Harteneck, E. G. Rightor, G. E. Mitchell, A. P. Hitchcock, L. Yang, T. Warwick, H. Ade, *J. Synchrotron Radiat.* **2003**, *10*, 125.
- [25] a) P. Giannozzi, S. Baroni, N. Bonini, M. Calandra, R. Car, C. Cavazzoni, D. Ceresoli, G. L. Chiarotti, M. Cococcioni, I. Dabo, A. Dal Corso, S. de Gironcoli, S. Fabris, G. Fratesi, R. Gebauer, U. Gerstmann, C. Gougoussis, A. Kokalj, M. Lazzeri, L. Martin-Samos, N. Marzari, F. Mauri, R. Mazzarello, S. Paolini, A. Pasquarello, L. Paulatto, C. Sbraccia, S. Scandolo, G. Sclauzero, A. P. Seitsonen, A. Smogunov, P. Umari, R. M. Wentzcovitch, *J. Phys.: Condens. Matter* **2009**, *21*, 395502; b) P. Giannozzi, O. Andreussi, T. Brumme, O. Bunau, M. Buongiorno Nardelli, M. Calandra, R. Car, C. Cavazzoni, D. Ceresoli, M. Cococcioni, N. Colonna, I. Carnimeo, A. Dal Corso, S. de Gironcoli, P. Delugas, R. A. DiStasio, A. Ferretti, A. Floris, G. Fratesi, G. Fugallo, R. Gebauer, U. Gerstmann, F. Giustino, T. Gorni, J. Jia, M. Kawamura, H. Y. Ko, A. Kokalj, E. Küçükbenli, M. Lazzeri, M. Marsili, N. Marzari, F. Mauri, N. L. Nguyen, H. V. Nguyen, A. Otero-de-la-Roza, L. Paulatto, S. Poncé, D. Rocca, R. Sabatini, B. Santra, M. Schlipf, A. P. Seitsonen, A. Smogunov, I. Timrov, T. Thonhauser, P. Umari, N. Vast, X. Wu, S. Baroni, *J. Phys.: Condens. Matter* **2017**, *29*, 465901.
- [26] J. P. Perdew, K. Burke, M. Ernzerhof, *Phys. Rev. Lett.* **1996**, *77*, 3865.
- [27] a) A. I. Liechtenstein, V. I. Anisimov, J. Zaanen, *Phys. Rev. B* **1995**, *52*, R5467; b) M. Cococcioni, S. de Gironcoli, *Phys. Rev. B* **2005**, *71*, 035105.
- [28] L. Wang, T. Maxisch, G. Ceder, *Phys. Rev. B* **2006**, *73*, 195107.
- [29] D. Vanderbilt, *Phys. Rev. B* **1990**, *41*, 7892.
- [30] a) Y. Liang, J. Vinson, S. Pemmaraju, W. S. Drisdell, E. L. Shirley, D. Prendergast, *Phys. Rev. Lett.* **2017**, *118*, 096402; b) Y. Liang, D. Prendergast, *Phys. Rev. B* **2018**, *97*, 205127.
- [31] M. Taillefumier, D. Cabaret, A.-M. Flank, F. Mauri, *Phys. Rev. B* **2002**, *66*, 195107.
- [32] a) D. Prendergast, G. Galli, *Phys. Rev. Lett.* **2006**, *96*, 215502; b) J.-J. Velasco-Velez, C. H. Wu, T. A. Pascal, L. F. Wan, J. Guo, D. Prendergast, M. Salmeron, *Science* **2014**, *346*, 831.